Emergence of Colloidal Patterns in ac Electric Fields

Florian Katzmeier, Bernhard Altaner⬤, Jonathan List⬤, Ulrich Gerland⬤, and Friedrich C. Simmel⬤

Physics Department E14 and T37, TU Munich, D-85748 Garching, Germany

Suspended microparticles subjected to ac electrical fields collectively organize into band patterns perpendicular to the field direction. The bands further develop into zigzag shaped patterns, in which the particles are observed to circulate. We demonstrate that this phenomenon can be observed quite generically by generating such patterns with a wide range of particles: silica spheres, fatty acid, oil, and coacervate droplets, bacteria, and ground coffee. We show that the phenomenon can be well understood in terms of second order electrokinetic flow, which correctly predicts the hydrodynamic interactions required for the pattern formation process. Brownian particle simulations based on these interactions accurately recapitulate all of the observed pattern formation and symmetry-breaking events, starting from a homogeneous particle suspension. The emergence of the formed patterns can be predicted quantitatively within a parameter-free theory.

Systems driven far from equilibrium can self-organize into spatiotemporal dissipative structures and thereby undergo spontaneous symmetry breaking [1,2]. Such dynamic behavior has been observed in electrokinetic experiments with clay particles [3], polystyrene microspheres [4], and also with λ-DNA [5]. When an alternating electric field is applied, particles form chains along the field direction, which move towards each other, align in parallel and develop extended band patterns roughly perpendicular to the field direction. The particle chains within the bands undergo dynamic breakup, resulting in the formation of triangular band structures wherein the particles circulate.

Originally, Jennings attributed the chain breakup to dipolelike repulsion forces arising from electrophoretic particle oscillations [3]. Hu *et al.* explained the particle circulation with electrorotation caused by mutual polarization of the particles [4]. Further experimental studies following this interpretation were conducted by Lele *et al.* [6] and Mittal *et al.* [7]. For observations with λ-DNA, Isambert and co-workers assumed that hydrodynamic interactions were generated by local conductivity gradients caused by electrophoretic salt depletion [5], resulting in liquid shearing under the influence of an external electric field. All of these models explained the dynamics within the band structures, but did not address their formation in the first place.

In the present Letter, we verify the generic emergence of the same characteristic patterns for a wide range of colloidal particles. We demonstrate that the observed phenomena can be naturally explained with an electrokinetic fluid flow [8–10] around the particles. A Brownian particle simulation accounting for the hydrodynamic and dipole-dipole pair interactions reproduces the key aspects of the band pattern formation, such as spontaneous

symmetry breaking, inclination of the bands, and particle circulation within these bands. For silica spheres, we experimentally investigate the emergence of patterns as a function of salt concentration and ac field frequency. The observed dependence can be predicted without any free parameters from the weakly nonlinear multi-scale theory of Schnitzer, Yariv, *et al.* [8,11].

Experiments.—We conducted our experiments with aqueous suspensions of various micrometer-scale particles, including fluorocarbon (FC) oil and lauric acid droplets, coacervates made from poly(allylamine) and adenosine triphosphate (ATP), monodisperse silica particles (radius $a \approx 650$ nm), *E. coli* bacteria, and ground coffee (experimental details and particle size distributions are given in the Supplemental Material [12]). The suspensions were loaded into microscope observation chambers with platinum electrodes placed at opposite inlets [see Fig. 1(a)]. After letting the colloids sediment for 10 min, we applied an in-plane ac electric field and recorded the resulting dynamics on the bottom of the chamber with an inverted microscope. We applied electric fields with amplitudes between 17 and 56 mV/μm, which is on the order of the thermal voltage ($\varphi_{\text{th}} := k_B T/e \approx 25.69$ mV) for μm sized particles. The applied frequency was set to 500 Hz for all samples except for bacteria, where it was 250 Hz.

We found that similar band patterns formed in all our samples (Fig. 1). Particle chain formation occurred within the first second after the electric field was switched on, while horizontal band structures emerged within the first minute. The band structures continued to grow and merge until the electric field was switched off. The time course of the pattern formation process is exemplarily shown for silica particles in Fig. 1(b), and can be clearly observed in the videos in the Supplemental Material [12]. Snapshots of
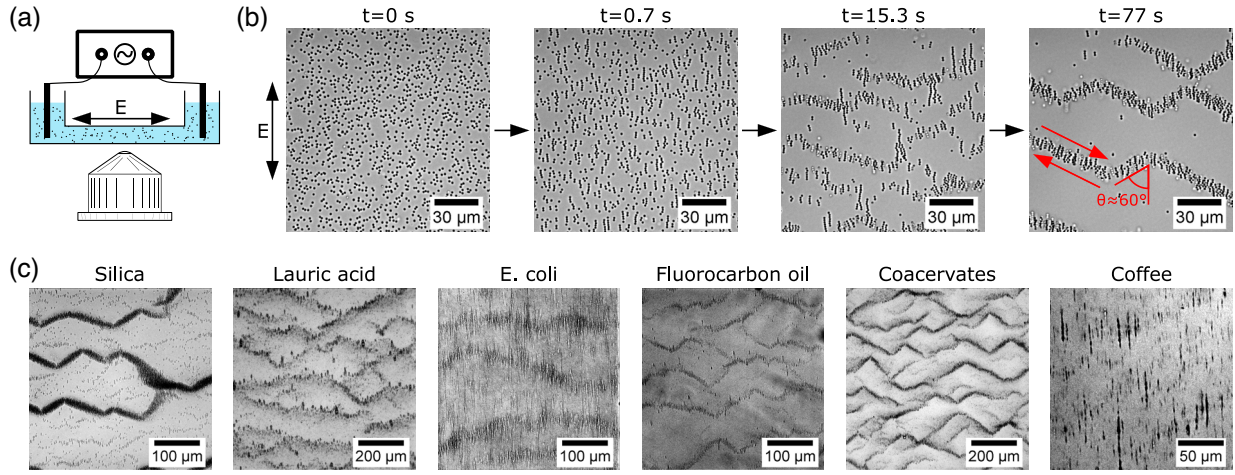
FIG. 1.   (a) Schematic representation of the experimental setup. Aqueous particle suspensions are subjected to ac electrical fields inside of a microscopic observation chamber. (b) Snapshots of a suspension of 1.3 μm diameter silica particles in an ac electric field ($E_0 = 17$ mV/μm, $f = 500$ Hz) at different time points. The formation of zigzag-shaped band patterns is clearly visible. In the fully formed bands ($t = 77$ s) the particles circulate as indicated. (c) Band formation and zigzag patterns in suspensions of various colloids. The images are taken $\approx$100 s after the electric field was turned on.

the patterns taken 100 s after the electric field was turned on are shown in Fig. 1(c). We observed distinct zigzag patterns for coacervates, FC oil, and silica particles, and less dominant patterns for the polydisperse lauric acid droplets. For the bacteria we found only chain formation at $f = 500$ Hz, while at $f = 250$ Hz the typical band patterns emerged, but less pronounced zigzag structures. The sample containing the polydisperse ground coffee particles showed more irregular behavior, but chain formation and also the onset of band formation could be clearly observed. The angle between the zigzag bands and the electric field axis was roughly 60° [highlighted in Fig. 1(b)].

Theoretical background.—The initially observed formation of particle chains is well known [3,4,6,7] and is caused by induced dipole-dipole interactions. When the external ac electric field is described as the real part of the complex phasor $\boldsymbol{E}(t) = E_0 e^{i\omega t}\hat{\boldsymbol{e}}_z$ with angular frequency $\omega = 2\pi f$, the time-averaged dipole-dipole force on a particle at position $\boldsymbol{r}$ exerted by another residing at the coordinate origin is given as

$$\boldsymbol{F}^{\mathrm{dip}}(\boldsymbol{r}) = 6\pi\epsilon|K_d|^2 E_0^2 a^2 \boldsymbol{h}(\boldsymbol{r}), \tag{1}$$

with the complex dipole coefficient K_d, the permittivity of water ϵ and the substitution $\boldsymbol{h}(\boldsymbol{r}) := [(1 - 3\cos^2\theta)/r^4]\hat{\boldsymbol{e}}_r - [(2\cos\theta\sin\theta)/r^4]\hat{\boldsymbol{e}}_\theta$ (θ is the zenith angle in spherical coordinates, and r is given in units of the particle radius a).

The formation of large scale patterns is driven by hydrodynamic interactions, which are caused by electrokinetic flow around the particles. The corresponding Poisson-Nernst-Planck-Navier-Stokes system of nonlinear partial differential equations can only be solved approximately [20–32]. For the dc case, Schnitzer, Yariv, *et al.* [8,11] recently developed a weakly nonlinear electrokinetic

theory, in which the dimensionless electrokinetic flow $\tilde{\boldsymbol{u}} := \boldsymbol{u}/u^*$, with $u^* = \{[(k_BT)^2\epsilon]/(e^2a\eta)\}$, is expanded in powers of the dimensionless electric field $\xi = [(ea)/(k_BT)]E_0$:

$$\tilde{\boldsymbol{u}} = \xi\tilde{\boldsymbol{u}}_1 + \xi^2\tilde{\boldsymbol{u}}_2 + \xi^3\tilde{\boldsymbol{u}}_3 + \cdots. \tag{2}$$

From the dc solution one can extrapolate to the time-averaged ac solution, where one can use the fact that odd powers of $\xi \propto E_0 e^{i\omega t}$ have a zero time average, which leaves $\tilde{\boldsymbol{u}}_2$ as the leading order electrokinetic flow. An explicit expression for $\tilde{\boldsymbol{u}}_2$ can be deduced from the stream function given in Ref. [8], which results in

$$\boldsymbol{u} = \frac{1}{2}u^*\xi^2\tilde{\boldsymbol{u}}_2 = u^*\xi^2\frac{\gamma}{2}(\boldsymbol{g} - \boldsymbol{h}), \tag{3}$$

where $\boldsymbol{g}(\boldsymbol{r}) := [(1 - 3\cos^2\theta)/r^2]\hat{\boldsymbol{e}}_r$ is a radial field and γ is a dimensionless microscopic parameter (see below and Ref. [8]). Notably, this well-known flow pattern [9,10] can be explicitly observed around large coacervate droplets via the trajectories of smaller droplets [Fig. 2(c), see also Supplemental Material, video [12]], which follow the streamlines of the electrokinetic flow shown in Fig. 2(b).

The derivation of the individual terms in Eq. (2) is quite involved [8,11], but the mechanism can be understood qualitatively from the scheme in Fig. 2: a negatively charged particle immersed in an electrolyte is surrounded by a diffuse charge layer (Debye layer), in which positive counterions are accumulated and co-ions are almost completely depleted. Outside the Debye layer the salt solution is electrically neutral. The asymmetry in ionic concentrations results in an ion-selective surface conductivity and surface current j_{Du}^+, which is characterized by the ion-selective Dukhin number Du [11].

In the electroneutral region, the electric field drives Ohmic counterionic and co-ionic currents $\boldsymbol{j}_E^+$ and $\boldsymbol{j}_E^-$ parallel
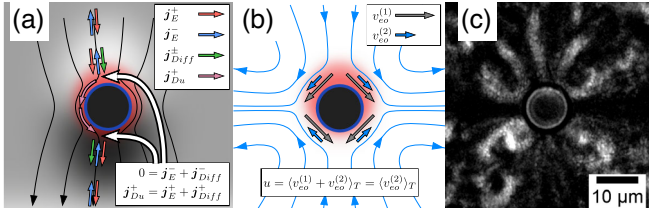
FIG. 2. (a) A charged particle in an electric field (black field lines) surrounded by counterions (red cloud) with ion fluxes (outlined arrows) along one field line. The neutral salt concentration is drawn as a gray cloud (darker regions correspond to higher concentrations). (b) Time averaged electrokinetic flow arising from Coulomb forces acting on the Debye layer. (c) Experimentally observed fluid motion around a large coacervate (superposition of a 3.8 s long video with enhanced contrast for moving particles). Bright areas correspond to trajectories of smaller coacervates.

to the field lines. Along field lines entering the Debye layer, flux balance requires a diffusion flux $\boldsymbol{j}_{\mathrm{diff}}$ which counterbalances the co-ion current $\boldsymbol{j}_E^-$. $\boldsymbol{j}_{\mathrm{diff}}$ can only result from a variation of the neutral salt concentration n in the vicinity of the colloid, which in Fig. 2(a) is depicted as a gray cloud with varying intensity. The electrokinetic properties of the Debye layer are determined by the zeta potential ζ, which depends on the surface charge and the extension of the Debye layer κ^{-1}, which in turn depends on n via $\kappa^{-1} = (2e^2 n/\epsilon k_B T)^{1/2}$. The variation of n outside the Debye layer causes a locally varying perturbation ζ_1 of the equilibrium zeta potential ζ_0, i.e., $\zeta = \zeta_0 + \zeta_1$, visualized as an expansion of the Debye layer on one side and a compression on the other side of the particle.

The free charges in the Debye layer are subject to a Coulomb force due to the tangential component of the electric field E_θ, which gives rise to fluid motion according to the electrokinetic slip boundary condition $v_{eo} = \zeta E_\theta$. The first and second order velocity components $v_{eo}^{(1)}$ and $v_{eo}^{(2)}$ connected to ζ_0 and ζ_1 are indicated in Fig. 2(b). For alternating electric fields $v_{eo}^{(1)}$ has a zero time average, while $v_{eo}^{(2)}$ has a nonvanishing time average, resulting in a fluid flow around the particle.

Brownian dynamics simulation.—In the overdamped limit, a direct force $\boldsymbol{F}_i^{\mathrm{tot}}$ exerted on particle i results in particle drift with velocity $[D_p/(k_B T)]\boldsymbol{F}_i^{\mathrm{tot}}$, where D_p is the diffusion constant of the particle. To include hydrodynamic interactions with the flow field $\boldsymbol{u}_i^{\mathrm{tot}}(\boldsymbol{r})$, which is caused by other particles ($j \neq i$) in the fluid, we use Faxen's correction for the drift velocity:

$$\boldsymbol{v}_i = \frac{D_p}{k_B T}\boldsymbol{F}_i^{\mathrm{tot}} + \left(1 + \frac{1}{6}\Delta\right)\boldsymbol{u}_i^{\mathrm{tot}}. \tag{4}$$

The direct force on particle i is obtained as the sum of dipolar and a repulsive interactions $\boldsymbol{F}^{\mathrm{rep}}(\boldsymbol{r}_{ij})$, i.e.,

$\boldsymbol{F}_i^{\mathrm{tot}} = \sum_{j \neq i}[\boldsymbol{F}^{\mathrm{dip}}(\boldsymbol{r}_{ij}) + \boldsymbol{F}^{\mathrm{rep}}(\boldsymbol{r}_{ij})]$, where $\boldsymbol{r}_{ij} = \boldsymbol{r}_i - \boldsymbol{r}_j$ denotes the difference vector between particles i and j. Ignoring geometric interactions, the velocity field caused by the particles $j \neq i$ is to zeroth order given as the sum $\boldsymbol{u}_i^{\mathrm{tot}} = \sum_{j \neq i}\boldsymbol{u}(\boldsymbol{r}_{ij})$. Together with Eqs. (1) and (3) and by recognizing that $\Delta \boldsymbol{g} = -6\boldsymbol{h}$ and $\Delta \boldsymbol{h} = 0$, the drift velocity [Eq. (4)] becomes

$$\boldsymbol{v}_i(\boldsymbol{r}_i) = u^* \sum_{j \neq i}\left[\xi^2\left(\frac{\gamma}{2}\boldsymbol{g}(\boldsymbol{r}_{ij}) + (|K_d|^2 - \gamma)\boldsymbol{h}(\boldsymbol{r}_{ij})\right) + \nu\boldsymbol{k}(\boldsymbol{r}_{ij})\right], \tag{5}$$

where the repulsion $\nu\boldsymbol{k}(\boldsymbol{r}_{ij})$ is discussed in Sec. 3 of Ref. [12]. The movement of the particles can then be described by the N-particle Langevin equation,

$$a\mathrm{d}\boldsymbol{r}_i = \boldsymbol{v}_i\mathrm{d}t + \sqrt{2D_p}\mathrm{d}W_i, \tag{6}$$

where $\mathrm{d}W$ is the increment of a Wiener process.

We numerically solved this stochastic differential equation with periodic boundary conditions and random initial particle configurations (Sec. 3 of Ref. [12]). As we observed the emergence of stripe patterns exclusively at the channel bottom, we restricted our simulation to two dimensions by constraining the dipole-dipole force and fluid flow to the plane $y = 0$, which captures both geometry and scaling of the physical interactions qualitatively correctly. As shown in Fig. 3, a simulation based on Eq. (6) with 1521 particles, $\gamma = 0.088$, $|K_d|^2 = 0.23$, and a particle number density matched to our silica particle experiments recapitulates all stages of the observed pattern formation process (cf. Fig. 1 and the Supplemental Material, video [12]; see Sec. 3 of Ref. [12] for a simulation with polydisperse particles.)

Parameter dependence.—To gain further insight into the physical mechanisms underlying the pattern formation process, we explored its dependence on ac field frequency and salt concentration. We prepared aqueous suspensions of silica particles at 0.0375% (w/v) with NaCl concentrations ranging from 5 to 2500 μM, and recorded microscopy videos with a relatively weak electric field amplitude of 10.6 mV$\,\mu$m^{-1} at frequencies ranging from 250 to 25 kHz. To analyze our data, we defined the "pattern visibility" p in an image as the discretized version of $p = \int_A |[\partial/(\partial z)](G * I)(x, z)|dxdz$, where A is the area of the image, G is a Gaussian with a standard deviation of 15 pixels (corresponding to 6 μm), $I(x, z)$ is the image intensity, and $*$ denotes convolution. The order parameter $p(t)$ is time dependent and measures density fluctuations along the z direction at a scale defined by G. We computed $p(t)$ for every frame of our microscopy videos and used it to determine a typical timescale τ_p for the emergence of stripe patterns [examples of $p(t)$ are shown in the Supplemental Material, Sec. II [12]]. In Fig. 4(a), τ_p^{-1} is
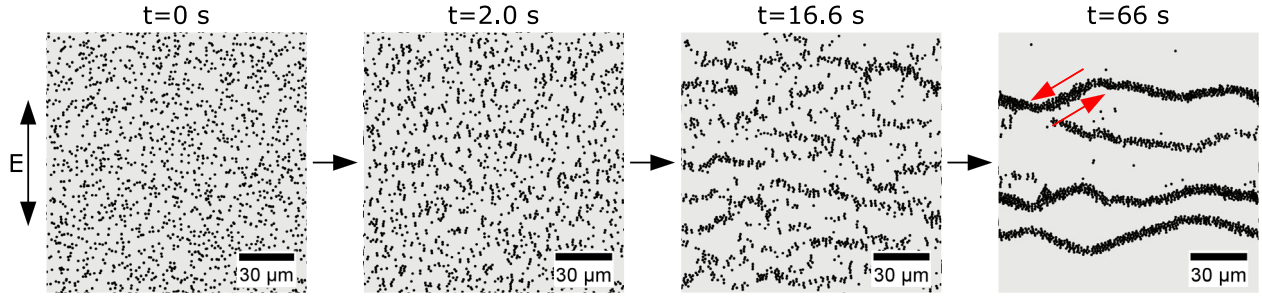
FIG. 3. Simulated dynamics with $\gamma = 0.088$ and $|K_d|^2 = 0.23$. Snapshots of a large scale simulation of the patterning process. The different stages of the experimentally observed patterning process from Fig. 1(b) are nicely reproduced. The particles circulate again as indicated.
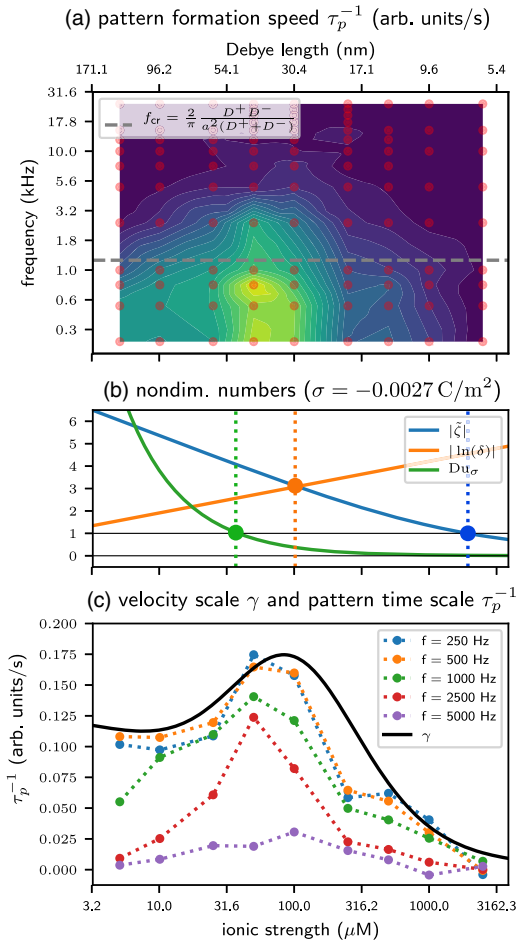

FIG. 4. (a) Observed pattern formation speed τ_p^{-1} in arbitrary units per time. Red circles indicate the experimental data points with a heat map generated by linear interpolation on the logarithmic grid. (b) Dimensionless characteristic numbers for electrokinetics lead to characteristic scales for the ionic strength (or, equivalently, Debye length), see main text for details. (c) The low-frequency pattern formation speed τ_p^{-1} can be quantitatively predicted without fit parameters using the second-order velocity scale γ derived by Schnitzer and Yariv in Ref. [8].

plotted as a measure for the speed of pattern formation for various frequencies and salt concentrations.

As electrokinetic fluid flow appears to drive the pattern formation process, we expect τ_p^{-1} to scale with the magnitude of the fluid flow, which is set by γ. The microscopic parameter γ is related to the physics of the Debye layer, whose details are specified by the curvature parameter $\delta := (\kappa a)^{-1}$ and the dimensionless equilibrium zeta potential $\tilde{\zeta}_0 = \zeta_0 / \varphi_{\text{th}}$ [8,11]. The latter is linked to the dimensionless surface charge density $\tilde{\sigma} := [\sigma / (\epsilon \kappa \varphi_{\text{th}})]$ by the Grahame equation $\tilde{\sigma} = 2 \sinh \tilde{\zeta}_0 / 2$. The ionic transport around colloidal particles is characterized by the Dukhin number Du, which measures the relative strength of surface to bulk conductivity [33–35]. By considering the surface conductivity of counter-ions only, an ion-selective Dukhin number [8,11] given by $\text{Du}_\sigma := \delta \tilde{\sigma}(1 + 2\mu^+)$ can be defined with the ionic drag coefficient $\mu^+ := [(\epsilon \varphi_{\text{th}}^2)/(\eta D^+)]$ and the counterion diffusion constant D^+ [8,11].

In Fig. 4(b), we show the variation of these dimensionless numbers for the ionic conditions of our experiment, where we set the surface charge to the known value for silica particles $\sigma = -0.0027 \text{ C/m}^2$ [36]. Comparison with Fig. 4(a) indicates that patterns can be observed only up to a characteristic ionic strength where $|\tilde{\zeta}_0|$ (blue dot) is $O(1)$. For higher ionic strengths, $|\zeta_0| < \varphi_{\text{th}}$, the physics of the Debye layer can be neglected altogether. Further, pattern formation is fastest when the zeta potential is "logarithmically large" compared to the curvature parameter, i.e., $|\tilde{\zeta}| = O(|\ln(\delta)|)$ (orange dot) and where surface conduction becomes dominant over bulk conduction, i.e., $\text{Du}_\sigma = O(1)$ (green dot).

Finally, in Fig. 4(c) we compare γ (Ref. [8]) with the observed pattern formation speed τ_p^{-1}, for which we scaled τ_p^{-1} such that its maximum at $f = 250$ Hz corresponds to the maximum value of γ. For the lowest experimental frequencies, we find excellent agreement between τ_p^{-1} and γ, and even for higher frequencies τ_p^{-1} qualitatively shows the same behavior, albeit with a reduced amplitude. Notably, the appearance of patterns for salt concentrations below 1 mM as well as the maximum pattern formation

speed at around 50 μM are nicely predicted by γ, when $\sigma = -0.0027$ C/m^2 is used. Further, we find that the value of γ chosen for our simulation (Fig. 3) has a physically reasonable magnitude. While no general nonlinear ac theory is available to date (a special case has recently been treated in Ref. [37]), we find that the decrease of the amplitude falls in the range of the characteristic frequency $f_{cr} = (2/\pi)[(D^+ D^-)/a^2(D^+ + D^-)] = 1.2$ kHz of the variation of neutral salt n, which is known from other linear ac theories [30,32,38–41]. As also expected from this model, both f_{cr} and τ_p^{-1} are reduced in experiments with higher viscosity (cf. Sec. 3.5 of Ref. [12]).

It remains to be explained why similar patterns emerge for widely different particle types even though the model predicting the hydrodynamic flow strictly applies only for hard spheres with a surface charge—except for the silica particles, the shape and interfacial structure of the investigated colloids is generally more complex (see also Sec. 3.8 of Ref. [12]). First, the geometry of the hydrodynamic flow is somewhat expected as it is the second order term of the general axisymmetric solution of the overdamped Navier-Stokes equation outside of a sphere [8,42,43]. Further, we expect the underlying mechanism to be generic to surface charge-stabilized colloidal dispersions [44], for which accumulation of counterions and depletion of co-ions close to the colloidal surface gives rise to an ion-selective surface conduction even for more complex surface compositions. Qualitatively, patterns are thus generally expected at low ionic strengths (< 1 mM) and low frequencies ($f < 1.2$ kHz) as predicted by the hard sphere model, and as used in the experiments of Fig. 1.

In conclusion, we experimentally verified the generic occurrence of a pattern formation process that had been previously observed when different types of colloids in aqueous suspension were subjected to ac electrical fields. We identified the physical mechanisms underlying the pattern forming process as dipole-dipole interactions and second order electrokinetic fluid flow, and confirmed the emergence of collective behavior in a many particle simulation. We found that Schnitzer-Yariv's weakly nonlinear electrokinetic theory gives a parameter-free quantitative explanation of the pattern formation process, which only requires a surface charge on the colloidal particles, providing a satisfactory unifying explanation for the observed macroscopic patterns and their underlying physical mechanism.

Apart from its fundamental scientific interest, the described effect could be utilized for applications in microfluidics and microrobotics. For instance, it should be possible to use the described electrokinetic flow to realize microfluidic pumps and mixers, as previously proposed based on induced charge electro-osmosis [45–50]. Further, our insights should be helpful for the development of electrically manipulated microswimmers, which were previously envisioned [51] and implemented [52–57]

based on inorganic (metallo-dielectric) Janus particles. Our experimental results with oil droplets, coacervates, lauric acid, and even bacteria demonstrate that similar swimmers consisting solely of soft and biological material are feasible.

[1] I. Prigogine and G. Nicolis, J. Chem. Phys. **46**, 3542 (1967).
[2] I. Prigogine and R. Lefever, J. Chem. Phys. **48**, 1695 (1968).
[3] B. R. Jennings and M. Stankiewicz, Proc. R. Soc. A **427**, 321 (1990).
[4] Y. Hu, J. L. Glass, A. E. Griffith, and S. Fraden, J. Chem. Phys. **100**, 4674 (1994).
[5] H. Isambert, A. Ajdari, J.-L. Viovy, and J. Prost, Phys. Rev. E **56**, 5688 (1997).
[6] P. P. Lele, M. Mittal, and E. M. Furst, Langmuir **24**, 12842 (2008).
[7] M. Mittal, P. P. Lele, E. W. Kaler, and E. M. Furst, J. Chem. Phys. **129**, 064513 (2008).
[8] O. Schnitzer, R. Zeyde, I. Yavneh, and E. Yariv, Phys. Fluids **25**, 052004 (2013).
[9] T. M. Squires and M. Z. Bazant, J. Fluid Mech. **509**, 217 (2004).
[10] Geoffrey Ingram Taylor, Proc. R. Soc. A **291**, 159 (1966).
[11] O. Schnitzer and E. Yariv, Phys. Rev. E **86**, 021503 (2012).
[12] See Supplemental Material at http://link.aps.org/supplemental/10.1103/PhysRevLett.128.058002 for videos accompanying Figs. 1–3, detailed materials and methods, experimental setup, experimental procedures, data and image analysis, details on theory and Brownian dynamics simulation, influence of the viscosity and particle size distribution, a discussion of the generality of the phenomenon, and Refs. [13–19].
[13] E. A. Frankel, P. C. Bevilacqua, and C. D. Keating, Langmuir **32**, 2041 (2016).
[14] E. Kopperger, J. List, S. Madhira, F. Rothfischer, D. C. Lamb, and F. C. Simmel, Science **359**, 296 (2018).
[15] Q. Tseng, I. Wang, E. Duchemin-Pelletier, A. Azioune, N. Carpi, J. Gao, O. Filhol, M. Piel, M. Théry, and M. Balland, Lab Chip **11**, 2231 (2011).
[16] T. Lindeberg, J. Appl. Stat. **21**, 225 (1994).
[17] A. Volk and C. J. Kähler, Exp. Fluids **59**, 75 (2018).
[18] N.-S. Cheng, Ind. Eng. Chem. Res. **47**, 3285 (2008).
[19] C. H. Li and C. K. Lee, Pattern Recognit. **26**, 617 (1993).
[20] J. J. Bikerman, Trans. Faraday Soc. **35**, 154 (1940).
[21] R. W. O'Brien and L. R. White, J. Chem. Soc., Faraday Trans. 2 **74**, 1607 (1978).
[22] R. W. O'Brien and R. J. Hunter, Can. J. Chem. **59**, 1878 (1981).
[23] R. O'Brien, J. Colloid Interface Sci. **92**, 204 (1983).

[24] J. H. Masliyah and S. Bhattacharjee, *Electrokinetic and Colloid Transport Phenomena* (Wiley-Interscience, Hoboken, N.J, 2006).

[25] S. S. Dukhin, *XXth International Congress of Pure and Applied Chemistry, International Union of Pure and Applied Chemistry* (Butterworths, London, 1965).

[26] P. Wiersema, A. Loeb, and J. Overbeek, J. Colloid Interface Sci. **22**, 78 (1966).

[27] H. Ohshima, T. W. Healy, and L. R. White, J. Chem. Soc., Faraday Trans. 2 **79**, 1613 (1983).

[28] H. Ohshima, Adv. Colloid Interface Sci. **62**, 189 (1995).

[29] H. Ohshima, *Theory of Colloid and Interfacial Electric Phenomena*, Interface Science and Technology Vol. 12 (Elsevier/Academic Press, Amsterdam, 2006).

[30] C. Grosse, J. Phys. Chem. B **116**, 13538 (2012).

[31] C. Grosse, J. Phys. Chem. B **113**, 8911 (2009).

[32] C. Grosse, J. Phys. Chem. B **113**, 11201 (2009).

[33] S. S. Dukhin, Adv. Colloid Interface Sci. **35**, 173 (1991).

[34] A. V. Delgado, F. González-Caballero, R. Hunter, L. K. Koopal, and J. Lyklema, Pure Appl. Chem. **77**, 1753 (2005).

[35] S. Dukhin, Adv. Colloid Interface Sci. **44**, 1 (1993).

[36] Y.-R. Shi, M.-P. Ye, L.-C. Du, and Y.-X. Weng, J. Phys. Chem. C **122**, 23764 (2018).

[37] R. Fernández-Mateo, P. García-Sánchez, V. Calero, H. Morgan, and A. Ramos, J. Fluid Mech. **924**, R2 (2021).

[38] V. Shilov, A. Delgado, F. Gonzalez-Caballero, and C. Grosse, Colloids Surf. A **192**, 253 (2001).

[39] J. Lyklema, S. S. Dukhin, and V. N. Shilov, J. Electroanal. Chem. Interfacial Electrochem. **143**, 1 (1983).

[40] J. Lyklema, M. M. Springer, V. N. Shilov, and S. S. Dukhin, J. Electroanal. Chem. Interfacial Electrochem. **198**, 19 (1986).

[41] C. Grosse and V. N. Shilov, J. Phys. Chem. **100**, 1771 (1996).

[42] M. J. Lighthill, Commun. Pure Appl. Math. **5**, 109 (1952).

[43] J. R. Blake, J. Fluid Mech. **46**, 199 (1971).

[44] B. Derjaguin and L. Landau, Prog. Surf. Sci. **43**, 30 (1993).

[45] M. Z. Bazant and Y. Ben, Lab Chip **6**, 1455 (2006).

[46] F. J. Hong, J. Cao, and P. Cheng, Int. Commun. Heat Mass Transfer **38**, 275 (2011).

[47] W. Y. Ng, S. Goh, Y. C. Lam, C. Yang, and I. Rodríguez, Lab Chip **9**, 802 (2009).

[48] C.-C. Huang, M. Z. Bazant, and T. Thorsen, Lab Chip **10**, 80 (2010).

[49] J. P. Urbanski, T. Thorsen, J. A. Levitan, and M. Z. Bazant, Appl. Phys. Lett. **89**, 143508 (2006).

[50] J. Wu, J. Appl. Phys. **103**, 024907 (2008).

[51] T. M. Squires and M. Z. Bazant, J. Fluid Mech. **560**, 65 (2006).

[52] S. Gangwal, O. J. Cayre, M. Z. Bazant, and O. D. Velev, Phys. Rev. Lett. **100**, 058302 (2008).

[53] C. Peng, I. Lazo, S. V. Shiyanovskii, and O. D. Lavrentovich, Phys. Rev. E **90**, 051002 (2014).

[54] T. Mano, J.-B. Delfau, J. Iwasawa, and M. Sano, Proc. Natl. Acad. Sci. U.S.A. **114**, E2580 (2017).

[55] D. Nishiguchi and M. Sano, Phys. Rev. E **92**, 052309 (2015).

[56] D. Nishiguchi, J. Iwasawa, H.-R. Jiang, and M. Sano, New J. Phys. **20**, 015002 (2018).

[57] A. Boymelgreen and G. Yossifon, Langmuir **31**, 8243 (2015).